Phys Chem Minerals
DOI 10.1007/s00269-008-0246-2

ORIGINAL PAPER

Stability at high-pressure, elastic behaviour and pressure-induced structural evolution of $CsAlSi_5O_{12}$, a potential host for nuclear waste

G. Diego Gatta · Nicola Rotiroti · Martin Fisch · Milen Kadiyski · Thomas Armbruster

Received: 14 January 2008 / Accepted: 29 April 2008

Abstract The elastic and structural behaviour of the synthetic zeolite $CsAlSi_5O_{12}$ (a = 16.753(4), b = 13.797(3) and c = 5.0235(17) Å, space group $Ama2$, $Z = 2$) were investigated up to 8.5 GPa by in situ single-crystal X-ray diffraction with a diamond anvil cell under hydrostatic conditions. No phase-transition occurs within the P-range investigated. Fitting the volume data with a third-order Birch–Murnaghan equation-of-state gives: $V_0 = 1{,}155(4)$ Å^3, $K_{T0} = 20(1)$ GPa and $K' = 6.5(7)$. The "axial moduli" were calculated with a third-order "linearized" BM-EoS, substituting the cube of the individual lattice parameter (a^3, b^3, c^3) for the volume. The refined axial-EoS parameters are: $a_0 = 16.701(44)$ Å, $K_{T0a} = 14(2)$ GPa ($\beta_a = 0.024(3)$ GPa^{-1}), $K'_a = 6.2(8)$ for the a-axis; $b_0 = 13.778(20)$ Å, $K_{T0b} = 21(3)$ GPa ($\beta_b = 0.016(2)$ GPa^{-1}), $K'_b = 10(2)$ for the b-axis; $c_0 = 5.018(7)$ Å, $K_{T0c} = 33(3)$ GPa ($\beta_c = 0.010(1)$ GPa^{-1}), $K'_c = 3.2(8)$ for the c-axis (K_{T0a}:K_{T0b}:K_{T0c} = 1:1.50:2.36). The HP-crystal structure evolution was studied on the basis of several structural refinements at different pressures: 0.0001 GPa (with crystal in DAC without any pressure medium), 1.58(3), 1.75(4), 1.94(6), 3.25(4), 4.69(5), 7.36(6), 8.45(5) and 0.0001 GPa (after decompression). The main deformation mechanisms at high-pressure are basically driven by tetrahedral tilting, the tetrahedra behaving as rigid-units. A change in the compressional mechanisms was observed at $P \leq 2$ GPa. The P-induced structural rearrangement up to 8.5 GPa is completely reversible. The high thermo-elastic stability of $CsAlSi_5O_{12}$, the immobility of Cs at HT/HP-conditions, the preservation of crystallinity at least up to 8.5 GPa and 1,000°C in elastic regime and the extremely low leaching rate of Cs from $CsAlSi_5O_{12}$ allow to consider this open-framework silicate as functional material potentially usable for fixation and deposition of Cs radioisotopes.

Keywords $CsAlSi_5O_{12}$ · Synthetic zeolite · Bikitaite · High-pressure · Compressibility · Equation-of-state · Nuclear waste disposal materials

G. D. Gatta (✉) · N. Rotiroti
Dipartimento di Scienze della Terra,
Università degli Studi di Milano, Via Botticelli 23,
20133 Milan, Italy
e-mail: diego.gatta@unimi.it

G. D. Gatta · N. Rotiroti
CNR-Istituto per la Dinamica dei Processi Ambientali,
Milan, Italy

M. Fisch · M. Kadiyski · T. Armbruster
Mineralogical Crystallography, Institute of Geological Sciences,
University of Bern, Freiestr. 3, 3012 Bern, Switzerland

Introduction

Cs-bearing minerals are extremely rare in Nature. Only a few structures of natural and synthetic Cs-aluminosilicates are known, such as pollucite ($CsAlSi_2O_6$, Newnham 1967; Beger 1969), Cs-rich beryl and pezzottaite [$Cs(Be_2Li)Al_2Si_6O_{18}$, Hawthorne et al. 2004], Cs-biotite (Hess and Fahey 1932) and nanpingite (Ni and Hughes 1996). Synthetic Cs-aluminosilicates have been prepared in the last decades in search for suitable crystalline phases potentially usable for fixation and deposition of radioactive isotopes of Cs, or as potential solid hosts for ^{137}Cs γ-radiation source to be used in sterilization applications (Vance and Seff 1975; Firor and Seff 1977; Gallagher et al. 1977; Klaska 1977; Araki 1980; Adl and Vance 1982; Komarneni and Roy 1983; Vance et al. 1984; Taylor et al. 1989; Mellini et al. 1996; Drábek et al. 1998; Comodi et al. 1999; Klika et al. 2006; Bubnova et al. 2007). Among those, the

synthesis conditions and the crystal structure of $CsAlSi_5O_{12}$, later described as CAS tetrahedral framework (Baerlocher et al. 2001), were reported by Araki (1980). Araki (1980) noticed a strong similarity in the construction scheme between the CAS framework and the structure of the natural zeolite bikitaite $Li_2Al_2Si_4O_{12}{\cdot}2H_2O$ (BIK topology, Baerlocher et al. 2001). Both structures have the secondary building unit (SBU) 5-1 (Baerlocher et al. 2001) but are distinct in the way these units are assembled to composite building units. BIK framework is only built by the "bik" composite building unit (CBU) whereas in CAS "bik" and "cas" CBUs are combined (Figs. 1, 2, 3). As noted by Araki (1980), there are also differences in the detailed shape of the eight-membered rings (8mR) in the two structures. In particular, how oxygen atoms wallpaper the inner surface of the one-dimensional channels. Annehed and Fälth (1984) synthesized $Cs_{0.70}[Al_{0.70}Si_{5.30}O_{12}]$ at 325°C under hydrothermal conditions and confirmed the BIK framework for this compound with Cs disordered over positions occupied by H_2O in bikitaite sensu strictu. There is the NSI framework type (Zanardi et al. 2004) with SBU 5-1 for which the "cas" and "bik" composite building units have also been identified (Baerlocher et al. 2001).

Si/Al-order in $CsAlSi_5O_{12}$ CAS has been studied with neutron powder diffraction and ^{29}Si MAS NMR by Hughes and Weller (2002), who reported that all Al is ordered at one tetrahedral site that is occupied by 50% Al and 50% Si. However, Fisch et al. (2008) disputed this interpretation and provide structural evidence (bond lengths and difference displacement parameters) for a random Si/Al-distribution over all tetrahedra. In addition, Fisch et al. (2008) demonstrated that $CsAlSi_5O_{12}$ CAS crystallizes at high temperature in space group *Amam* (*Cmcm* in standard setting), which is the highest topological symmetry of CAS, and transforms below 500°C by a displacive mechanism to space group *Ama*2. Consequently, at room temperature all the *Ama*2 crystals are twinned in a 1:1 ratio by the inversion operation.

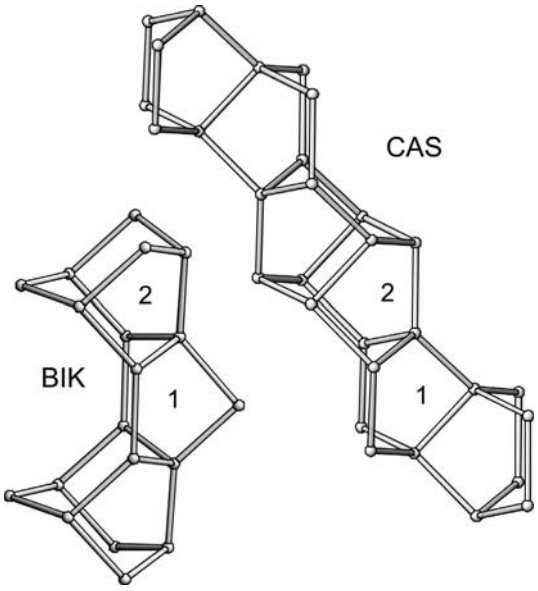

Fig. 1 Arrangement of secondary building units (SBU) 5-1 in the CAS and BIK frameworks (only connections between T sites are drawn). Topologically identical fragments are marked by *numbers*

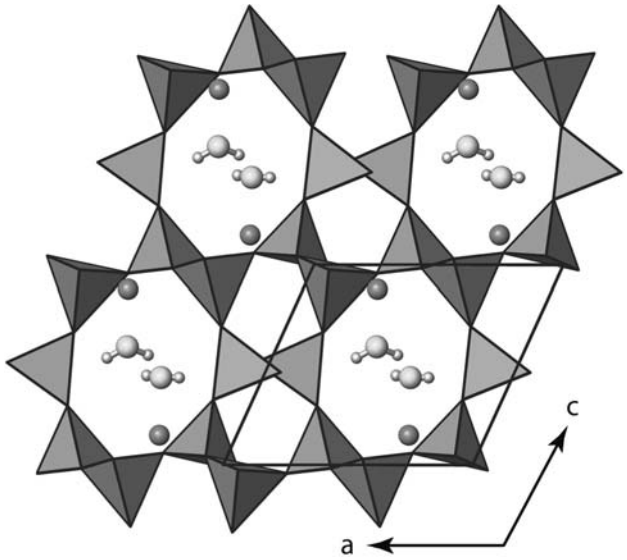

Fig. 2 The crystal structure of bikitaite, $Li_2Al_2Si_4O_{12}{\cdot}2H_2O$, viewed down [010]. The extra-framework content is represented by Li-sites (*dark-grey spheres*) and H_2O molecules (*light-grey*). The water molecules form one dimensional chains along [010] (Fois et al. 1999; Comodi et al. 2003)

For bikitaite, two modifications are described: monoclinic bikitaite with Si/Al-disordered in the tetrahedra forming puckered six-membered ring sheets (e.g. Kocman et al. 1974) and triclinic bikitaite with ordered Si/Al-distribution in the corresponding tetrahedra (e.g. Bissert and Liebau 1986). For the same axial orientation for BIK and CAS, the maximum BIK topological symmetry becomes *Ccmm*, indicating that in CAS (*Amam*) and BIK face-centering occurs in different directions.

The elastic and *P*-induced main deformation mechanisms in natural triclinic bikitaite ($a \sim 8.607$ Å, $b \sim 4.956$ Å, $c \sim 7.608$ Å, $\alpha \sim 89.92°$, $\beta \sim 114.38°$ and $\gamma \sim 89.83°$, space group *P*1) were investigated by Comodi et al. (2003) and Gatta et al. (2003) by in situ X-ray single-crystal diffraction up to 4 GPa, and by Ferro et al. (2002) on the basis of synchrotron powder diffraction up to 10 GPa and ab initio molecular dynamics simulations. Using non-penetrating *P*-media, bikitaite does not experience any *P*-induced phase-transition at least up to 10 GPa. A strong anisotropic compression was observed in natural bikitaite, being $\beta_a{:}\beta_b{:}\beta_c = 1{:}2.75{:}3.90$ (Comodi et al. 2003, Gatta et al. 2003). The isothermal bulk modulus of bikitaite, calculated with a second-order Birch-Murnaghan equation-of-state, is

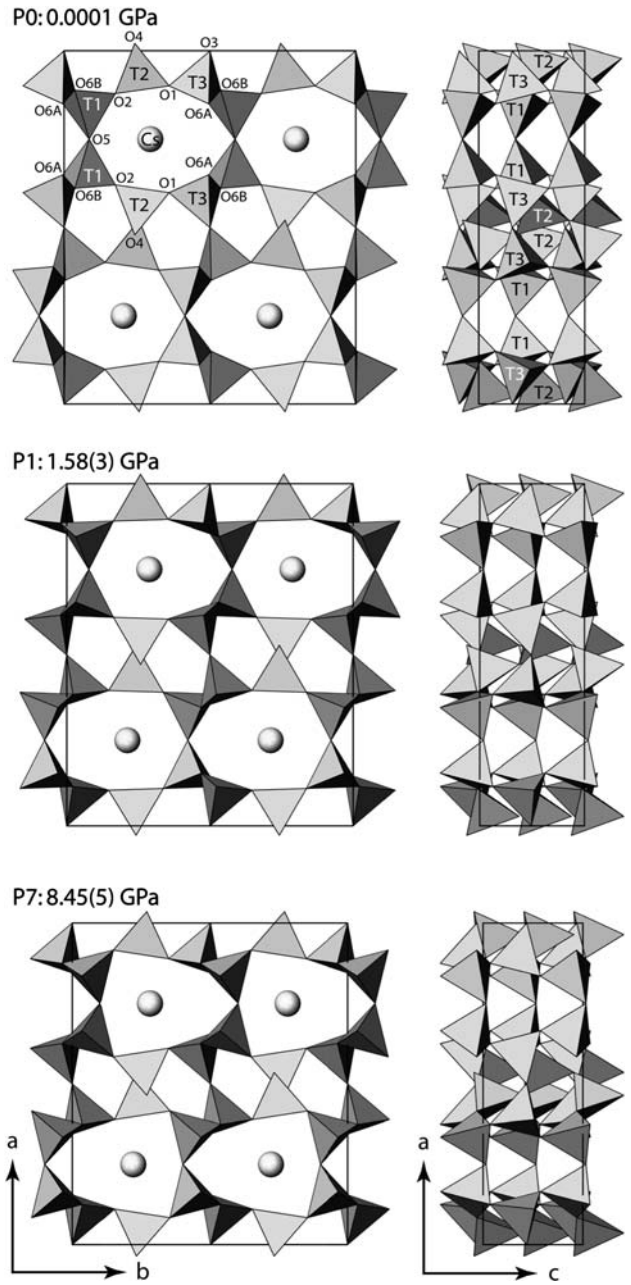

Fig. 3 Unit cell of $CsAlSi_5O_{12}$ projected along *c*-axis (*left*) and *b*-axis (*right*) at P_0, P_1 and P_7 (*top to bottom*). Atoms are labelled according to the structural refinements (Table 1). For easier illustration, Cs is not shown in the projections along the *b*-axis. A drastic structural change occurs between P_0 to P_1: O5 is shifted along the *c*-axis due to rigid-body tetrahedral rotation

$K_{T0} = 44.2(4)$ GPa (Comodi et al. 2003; Gatta et al. 2003). Due to the low quality of the diffraction data at high-pressure, only one structural refinement of bikitaite at 3.2 GPa was performed using single-crystal diffraction data (Comodi et al. 2003). Bikitaite has an unusual structural feature: the presence of a one-dimensional H_2O chain running along the [010] 8-membered ring channel (Fois et al. 1999). Based on ab initio molecular dynamics simulations, Ferro et al. (2002) showed that compression brings framework oxygen atoms close enough to water hydrogen atoms to allow the formation of host–guest hydrogen bonds, whilst still preserving the one-dimensional chains. However, the general configuration of the Si/Al-framework is maintained at least up to 10 GPa.

The aim of the present study was to investigate the elastic behaviour and *P*-induced structural evolution of $CsAlSi_5O_{12}$ by means of in situ single-crystal X-ray diffraction with a diamond anvil cell. A comparison with the thermal behaviour of this synthetic zeolite (Fisch et al. 2008) and the elastic behaviour of the natural bikitaite (Ferro et al. 2002; Comodi et al. 2003; Gatta et al. 2003) is also discussed.

Experimental methods

A crystalline sample of $CsAlSi_5O_{12}$ was synthesized by slow cooling of the starting oxides in a $BaO–V_2O_5$ flux from 1,420 to 750°C. Some single-crystals were separated from the flux by rinsing with hot NaOH solution. Their composition was determined using a Jeol JX-8200 electron microprobe. Synthetic $CsVO_3$, natural $Ba(SO_4)$, $K(AlSi_3O_8)$, and $Ca(Al_2Si_2O_8)$ were used as standards. The average crystal composition was $Cs_{0.85}Al_{0.85}Si_{5.15}O_{12}$ (see Fisch et al. 2008 for further details). Deviation from ideal $CsAlSi_5O_{12}$ composition is in accordance with previous findings (Ito 1976; Araki 1980).

One platy crystal of $CsAlSi_5O_{12}$ ($210 \times 140 \times 60$ μm^3), free of defects on the optical scale, was selected for X-ray diffraction experiments. Diffraction data were first collected at room conditions with an Oxford Diffraction—Xcalibur-1 diffractometer equipped with CCD, using a graphite monochromator for Mo*K*α-radiation, operated at 50 kV and 40 mA. In order to maximize the reciprocal space coverage, a combination of ω and φ scans was used, with a step size of 0.4° and a time of 30 s/frame (Table 1). The distance between the crystal and the detector was 80 mm. 12071 Bragg reflections were collected in the range $2 < 2\theta < 65°$, of which 1562 were unique with $F_o > 4\sigma(F_o)$ (Table 1), giving a metrically orthorhombic lattice with $a = 16.753(4)$, $b = 13.797(3)$, and $c = 5.0235(17)$ Å. After Lorentz-polarization (Lp) and analytical absorption corrections using the CrysAlis package (Oxford Diffraction 2005), by Gaussian integration based upon the shape and dimensions of the crystal, the discrepancy factor among symmetry-related reflections (Laue class *mmm*) was $R_{int} = 0.058$ (Table 1). The reflection absences were consistent with space group *Amam* and *Ama*2. The structural refinement was performed with anisotropic displacement parameters using the SHELX-97 software (Sheldrick 1997), starting from the atomic coordinates of Araki (1980) transformed to the space group *Ama*2. The refined Flack parameter was $x = 0.50(3)$,

Table 1 Details pertaining to the data collection and refinement of $CsAlSi_5O_{12}$ at different pressures

P (GPa)	0.0001	0.0001[a] (P_0)	1.58(3) (P_1)	1.75(4) (P_2)	1.94(6) (P_3)	3.25(4) (P_4)	4.69(5) (P_5)	7.36(6) (P_6)	8.45(5) (P_7)	0.0001[b]
Diffractometer	Xcalibur CCD	Xcalibur CCD	Xcalibur CCD	Xcalibur CCD	Xcalibur CCD	Xcalibur CCD	Xcalibur CCD	Xcalibur CCD	Xcalibur CCD	Xcalibur CCD
X-ray radiation	Mo$K\alpha$	Mo$K\alpha$	Mo$K\alpha$	Mo$K\alpha$	Mo$K\alpha$	Mo$K\alpha$	Mo$K\alpha$	Mo$K\alpha$	Mo$K\alpha$	Mo$K\alpha$
Scan type	ω/φ	ω/φ	ω/φ	ω/φ	ω/φ	ω/φ	ω/φ	ω/φ	ω/φ	ω/φ
Scan width (°/frame)	0.4	0.4	0.4	0.4	0.4	0.4	0.4	0.4	0.4	0.4
Exposure (s/frame)	30	30	30	30	30	30	30	30	30	30
Temperature (K)	298	298	298	298	298	298	298	298	298	298
Space group	*Ama*2	*Ama*2	*Ama*2	*Ama*2	*Ama*2	*Ama*2	*Ama*2	*Ama*2	*Ama*2	*Ama*2
Cell dim. (Å)										
a	16.753(4)	16.733(3)	16.203(2)	16.155(3)	16.110(4)	15.914(5)	15.664(4)	15.357(3)	15.241(4)	16.754(2)
b	13.797(3)	13.776(17)	13.527(15)	13.48(2)	13.48(3)	13.34(4)	13.21(2)	13.03(3)	13.00(3)	13.7993(19)
c	5.0235(17)	5.0104(5)	4.9488(6)	4.9397(7)	4.9268(8)	4.878(1)	4.820(1)	4.737(1)	4.7154(7)	5.0144(9)
Z	2	2	2	2	2	2	2	2	2	2
Maximum 2θ (°)	65	60	60	60	60	60	60	60	60	65
Measured reflections	12,071	2,506	2,301	2,395	2,294	2,262	2,149	2,074	2,043	11,839
Unique reflections	2,022	345	253	263	256	246	254	247	240	1,727
Unique reflections with $F_o > 4\sigma(F_o)$	1,562	332	243	250	250	237	244	237	233	1,501
R_{int}	0.0582	0.0462	0.0645	0.0683	0.0639	0.0918	0.0476	0.0482	0.0597	0.0693
Number of l.s. parameters	91	33	33	33	33	33	33	33	33	91
R_1, $F_o > 4\sigma(F_o)$	0.0491	0.0624	0.0861	0.0871	0.0967	0.083	0.0828	0.0768	0.0748	0.0625
R_1, all data	0.0773	0.0694	0.0905	0.1136	0.0988	0.0958	0.0843	0.0798	0.0770	0.0780
GooF	1.049	1.106	1.188	1.101	1.155	1.171	1.084	1.121	1.095	1.074

[a] With the crystal in the DAC without *P*-medium

[b] With the crystal in air after decompression

Table 2 Atomic coordinates and displacement parameters (Å^2) of $CsAlSi_5O_{12}$ at different pressures

Sites	*P* (GPa)	*x*	*y*	*z*	Uiso, Ueq
Cs	0.0001	0.25	0.20384(5)	0	0.0647(3)
	0.0001[a]	0.25	0.2045(6)	0	0.0742(12)
	1.58(3)	0.25	0.2118(6)	0	0.0332(9)
	1.75(4)	0.25	0.2139(8)	0	0.0318(12)
	1.94(4)	0.25	0.2162(7)	0	0.0310(10)
	3.25(4)	0.25	0.2157(7)	0	0.0299(10)
	4.69(5)	0.25	0.2166(6)	0	0.0242(9)
	7.36(6)	0.25	0.2194(5)	0	0.0195(8)
	8.45(5)	0.25	0.2197(5)	0	0.0214(8)
	0.0001[b]	0.25	0.20377(6)	0	0.0627(4)
T1	0.0001	0.15713(5)	0.42606(7)	0.41683(3)	0.0181(2)
	0.0001[a]	0.15746(18)	0.4267(7)	0.4202(9)	0.0176(5)
	1.58(3)	0.1580(5)	0.4398(12)	0.4365(17)	0.0416(15)
	1.75(4)	0.1581(6)	0.4387(15)	0.435(2)	0.050(2)
	1.94(4)	0.1582(6)	0.4403(14)	0.4336(19)	0.0412(19)
	3.25(4)	0.1578(6)	0.4400(13)	0.4241(18)	0.0425(18)
	4.69(5)	0.1591(6)	0.4409(16)	0.4153(19)	0.0424(18)
	7.36(6)	0.1585(6)	0.4381(16)	0.405(2)	0.0397(16)
	8.45(5)	0.1584(6)	0.4379(17)	0.402(2)	0.0412(15)
	0.0001[b]	0.15702(6)	0.42609(8)	0.4151(4)	0.0170(3)
T2	0.0001	0.05302(6)	0.74116(7)	0.0417(3)	0.0184(2)
	0.0001[a]	0.05325(17)	0.7410(7)	0.0445(9)	0.0176(5)
	1.58(3)	0.0534(5)	0.7453(11)	0.0641(19)	0.0416(15)
	1.75(4)	0.0533(6)	0.7452(13)	0.062(2)	0.050(3)
	1.94(4)	0.0529(6)	0.7471(12)	0.0635(19)	0.0412(19)
	3.25(4)	0.0532(6)	0.7473(12)	0.0677(18)	0.0425(18)
	4.69(5)	0.0531(6)	0.7461(13)	0.0723(19)	0.0424(18)
	7.36(6)	0.0539(5)	0.7495(13)	0.079(2)	0.0397(16)
	8.45(5)	0.0542(5)	0.7495(15)	0.082(2)	0.0412(15)
	0.0001[b]	0.05288(7)	0.74121(9)	0.0411(4)	0.0175(3)
T3	0.0001	0.08961(5)	0.02674(7)	0.4017(3)	0.0184(2)
	0.0001[a]	0.08973(19)	0.0286(7)	0.4033(9)	0.0176(5)
	1.58(3)	0.0927(4)	0.0329(13)	0.4380(19)	0.0416(15)
	1.75(4)	0.0942(6)	0.0324(14)	0.433(2)	0.050(2)
	1.94(4)	0.0933(5)	0.0342(14)	0.4330(19)	0.0412(19)
	3.25(4)	0.0947(5)	0.0353(14)	0.4242(18)	0.0425(18)
	4.69(5)	0.0955(6)	0.0334(15)	0.4170(18)	0.0424(18)
	7.36(6)	0.0976(6)	0.0369(14)	0.405(2)	0.0397(16)
	8.45(5)	0.1000(5)	0.0369(15)	0.401(2)	0.0412(15)
	0.0001[b]	0.08936(7)	0.02676(8)	0.4005(4)	0.0176(3)
O1	0.0001	0.09908(16)	0.1400(2)	0.4766(8)	0.0378(9)
	0.0001[a]	0.0990(6)	0.1403(7)	0.483(2)	0.0386(15)
	1.58(3)	0.1044(10)	0.1465(10)	0.521(5)	0.082(5)
	1.75(4)	0.1047(10)	0.1463(11)	0.519(5)	0.084(5)
	1.94(4)	0.1052(11)	0.1481(11)	0.519(5)	0.077(6)
	3.25(4)	0.1072(11)	0.1492(11)	0.522(5)	0.085(6)
	4.69(5)	0.1090(12)	0.1479(14)	0.519(7)	0.059(4)
	7.36(6)	0.1125(10)	0.1529(13)	0.506(6)	0.039(2)
	8.45(5)	0.1109(11)	0.1519(14)	0.513(6)	0.056(3)
	0.0001[b]	0.0995(2)	0.1409(3)	0.4740(11)	0.0359(12)
O2	0.0001	0.1219(2)	0.3235(2)	0.5162(9)	0.0471(9)
	0.0001[a]	0.1208(5)	0.3244(8)	0.512(2)	0.0386(15)
	1.58(3)	0.1095(12)	0.3369(13)	0.474(5)	0.082(5)
	1.75(4)	0.1092(12)	0.3379(14)	0.481(6)	0.084(5)
	1.94(4)	0.1067(13)	0.3396(14)	0.468(5)	0.077(6)
	3.25(4)	0.1008(13)	0.3432(14)	0.460(5)	0.085(6)
	4.69(5)	0.1033(14)	0.3417(16)	0.456(5)	0.059(4)
	7.36(6)	0.0867(13)	0.3522(16)	0.439(4)	0.039(2)
	8.45(5)	0.0842(15)	0.3526(17)	0.438(5)	0.056(3)
	0.0001[b]	0.1222(3)	0.3238(3)	0.5117(13)	0.0456(12)
O3	0.0001	0	0	0.3143(10)	0.0361(11)
	0.0001[a]	0	0	0.316(3)	0.0386(15)
	1.58(3)	0	0	0.492(7)	0.082(5)
	1.75(4)	0	0	0.473(7)	0.084(5)
	1.94(4)	0	0	0.482(7)	0.077(6)
	3.25(4)	0	0	0.466(7)	0.085(6)
	4.69(5)	0	0	0.457(8)	0.059(4)
	7.36(6)	0	0	0.444(5)	0.039(2)
	8.45(5)	0	0	0.438(7)	0.056(3)
	0.0001[b]	0	0	0.3065(17)	0.0352(15)
O4	0.0001	0.02304(18)	0.7395(3)	0.3502(6)	0.0360(8)
	0.0001[a]	0.0212(5)	0.7424(14)	0.348(2)	0.0386(15)
	1.58(3)	0.0278(11)	0.7578(19)	0.375(4)	0.082(5)
	1.75(4)	0.0277(10)	0.756(2)	0.376(3)	0.084(5)
	1.94(4)	0.0292(11)	0.7585(19)	0.378(4)	0.077(6)
	3.25(4)	0.0325(10)	0.761(2)	0.390(4)	0.085(6)
	4.69(5)	0.0335(12)	0.761(3)	0.396(4)	0.059(4)
	7.36(6)	0.0360(11)	0.767(3)	0.408(3)	0.039(2)
	8.45(5)	0.0358(12)	0.769(3)	0.410(4)	0.056(3)
	0.0001[b]	0.0234(2)	0.7392(4)	0.3486(10)	0.0355(11)
O5	0.0001	0.25	0.4120(4)	0.3491(12)	0.0609(18)
	0.0001[a]	0.25	0.4140(19)	0.347(3)	0.0386(15)
	1.58(3)	0.25	0.423(3)	0.536(5)	0.082(5)
	1.75(4)	0.25	0.421(3)	0.534(6)	0.084(5)
	1.94(4)	0.25	0.421(3)	0.535(6)	0.077(6)
	3.25(4)	0.25	0.412(3)	0.530(6)	0.085(6)
	4.69(5)	0.25	0.413(4)	0.544(7)	0.059(4)
	7.36(6)	0.25	0.406(4)	0.537(6)	0.039(2)
	8.45(5)	0.25	0.400(4)	0.531(8)	0.056(3)
	0.0001[b]	0.25	0.4125(7)	0.344(2)	0.062(3)
O6A	0.0001	0.14846(16)	0.0067(2)	0.1511(7)	0.0353(8)
	0.0001[a]	0.1495(5)	0.0041(11)	0.1578(19)	0.0386(15)
	1.58(3)	0.1154(16)	0.0218(16)	0.124(3)	0.082(5)
	1.75(4)	0.1190(16)	0.0249(17)	0.117(3)	0.084(5)
	1.94(4)	0.1137(16)	0.0248(17)	0.118(3)	0.077(6)
	3.25(4)	0.1222(18)	0.0291(16)	0.109(3)	0.085(6)
	4.69(5)	0.122(2)	0.032(2)	0.095(3)	0.059(4)
	7.36(6)	0.1231(15)	0.0353(19)	0.075(3)	0.039(2)
	8.45(5)	0.1254(19)	0.0369(19)	0.071(3)	0.056(3)
	0.0001[b]	0.1485(2)	0.0069(3)	0.1501(11)	0.0367(12)

Table 2 continued

Sites	*P* (GPa)	*x*	*y*	*z*	Uiso, Ueq
O6B	0.0001	0.1122(3)	0.4596(3)	0.1509(8)	0.0554(11)
	0.0001[a]	0.1112(6)	0.4633(12)	0.1594(19)	0.0386(15)
	1.58(3)	0.1543(11)	0.4692(17)	0.123(3)	0.082(5)
	1.75(4)	0.1547(12)	0.4675(18)	0.119(3)	0.084(5)
	1.94(4)	0.1554(12)	0.4701(18)	0.118(3)	0.077(6)
	3.25(4)	0.1579(12)	0.4693(18)	0.107(3)	0.085(6)
	4.69(5)	0.1629(14)	0.470(3)	0.097(4)	0.059(4)
	7.36(6)	0.1648(12)	0.468(2)	0.079(3)	0.039(2)
	8.45(5)	0.1654(13)	0.465(2)	0.074(4)	0.056(3)
	0.0001[b]	0.1110(4)	0.4595(4)	0.1514(13)	0.0539(15)

The H*P*-structure refinements were conducted with the occupancy of the Cs-site fixed to the value refined with the crystal in air (i.e. 80.9(3)%)

Note: Anisotropic refinements have been performed only with the crystal in air. *U*eq are given for the anisotropic refinements, *U*iso for the isotropic refinements

[a] With the crystal in the DAC without *P*-medium

[b] With the crystal in air after decompression

as expected for racemic twin (i.e. individuals in a 1:1 ratio by the inversion operation); then, the intensity data have been corrected for twinning. Neutral atomic scattering factors of Cs, Si and O from the International Tables for Crystallography (Wilson and Prince 1999) were used. Due to the low Al content of the tetrahedral framework, the use of a scattering curve based on partially occupied tetrahedral sites (by Al and Si) did not improve the figures of merit of the refinement. According to Araki (1980), the Cs-site was found to be partially occupied [80.9(3)%]. No peak larger than ± 0.98 $e^{-}/Å^3$ was present in the final difference-Fourier synthesis at the end of the refinement. Details of the ambient structural refinement are reported in Tables 1, 2, 3 and 4.

An ETH-type diamond anvil cell (DAC, Miletich et al. 2000) was used for the high-pressure experiments. Steel T301 foil, 250 μm thick, was used as gasket. The gasket foil was pre-indented to a thickness of about 120 μm before drilling a hole (Ø 350 μm) by spark-erosion. The same crystal of $CsAlSi_5O_{12}$ as that studied at ambient conditions was placed into the gasket hole together with a single-crystal of quartz used for pressure measurement (Angel et al. 1997). A methanol:ethanol (4:1) mixture was used as hydrostatic pressure-transmitting medium (Angel et al. 2007). Accurate lattice parameters were determined at pressures ranging between 0.0001 and 8.45(5) GPa (Table 1) with a KUMA-KM4 diffractometer, equipped with a point-detector and monochromatised Mo*K*α-radiation, using 28 Bragg reflections. Data collections at 0.0001 GPa (crystal in DAC without any pressure medium, P_0), 1.58(3) (P_1), 1.75(4) (P_2), 1.94(6) (P_3), 3.25(4) (P_4), 4.69(5) (P_5), 7.36(6) (P_6), and 8.45(5) GPa (P_7) (Table 1) were performed using an Xcalibur-1 diffractometer (Oxford Diffraction) equipped with a CCD, adopting the same experimental set-up and the same data collection strategy as that used with the crystal in air (Table 1). No violation of the reflection conditions of *Ama*2 symmetry were observed at any pressure. Integrated intensity data were corrected for Lp and absorption effects due to the crystal and the DAC using the ABSORB 5.2 computer program (Burnham 1966; Angel 2002). The structure refinements were conducted with the occupancy of the Cs-site fixed to the value refined with the crystal in air [80.9(3)%]. Soft geometrical restraints were used to restrain tetrahedral T–O and O–O distances to those obtained at room-pressure (air): T–O distances were restrained to a target value of 1.60 Å with an estimated standard deviation of ±0.015 Å and the tetrahedral O–O distances to 2.60 ± 0.04 Å. The stability of the H*P*-refinements is improved by the soft restrains adopted, which act as if they were some additional experimental observations (Gatta et al. 2006, Sheldrick 1997). In order to reduce the number of the refined variables, the isotropic

Table 3 Inter-tetrahedral bond angles (°) at different pressures

P (GPa)	T2–O1–T3	T1–O2–T2	T3–O3–T3	T2–O4–T2	T1–O5–T1	T3–O6A–T1	T3–O6B–T1
0.0001	146.06(19)	153.9(3)	148.4(4)	143.7(2)	151.8(4)	137.12(19)	158.4(3)
0.0001[a]	146.1(7)	156.7(7)	149(1)	147.1(8)	150(1)	138.9(9)	159(1)
1.58(3)	141(1)	168(2)	161(2)	140(1)	140(2)	136(1)	135(1)
1.75(4)	142(1)	172(2)	166(2)	140(1)	140(2)	133(1)	135(1)
1.94(4)	141(1)	168(2)	163(2)	138(1)	138(2)	135(1)	135(1)
3.25(4)	139(1)	166(2)	165(3)	133(1)	133(2)	133(1)	132(1)
4.69(5)	138(2)	166(2)	166(3)	132(1)	127(2)	129(2)	129(1)
7.36(6)	137(1)	150(2)	167(2)	128(1)	124(2)	126(1)	127(1)
8.45(5)	140(1)	148(2)	168(2)	128(1)	121(2)	124(1)	126(1)
0.0001[b]	145.3(3)	154.3(4)	146.0(6)	143.4(3)	150.9(6)	136.8(3)	157.6(4)

[a] With the crystal in the DAC without *P*-medium

[b] With the crystal in air after decompression

Table 4 T–O bond lengths (Å) at various pressures (GPa)

Tetrahedron	Ligand	0.0001	0.0001[a]	1.58(3)	1.75(4)	1.94(4)	3.25(4)	4.69(5)	7.36(6)	8.45(5)	0.0001[b]
T1	O2	1.612(3)	1.605(11)	1.610(13)	1.591(14)	1.600(13)	1.588(13)	1.587(14)	1.579(14)	1.594(14)	1.603(4)
	O5	1.6042(16)	1.601(5)	1.586(10)	1.582(11)	1.583(11)	1.599(11)	1.594(13)	1.596(13)	1.601(13)	1.609(2)
	O6A	1.626(3)	1.604(10)	1.602(13)	1.599(13)	1.597(13)	1.597(14)	1.592(14)	1.596(15)	1.597(15)	1.628(4)
	O6B	1.601(4)	1.601(8)	1.602(12)	1.608(12)	1.605(12)	1.596(12)	1.585(13)	1.594(12)	1.587(13)	1.598(6)
<T1–O>		1.611(3)	1.603(9)	1.600(12)	1.595(13)	1.596(12)	1.595(13)	1.590(14)	1.591(14)	1.595(14)	1.610(4)
T2	O1	1.627(3)	1.614(11)	1.587(13)	1.585(13)	1.593(13)	1.582(14)	1.587(14)	1.586(14)	1.570(17)	1.625(4)
	O2	1.624(3)	1.620(10)	1.600(13)	1.591(13)	1.590(13)	1.578(14)	1.589(14)	1.577(15)	1.572(18)	1.633(4)
	O4	1.629(3)	1.611(9)	1.604(13)	1.611(13)	1.602(13)	1.616(14)	1.602(14)	1.599(13)	1.589(17)	1.620(5)
	O4	1.619(3)	1.605(8)	1.614(11)	1.599(11)	1.611(11)	1.620(12)	1.603(12)	1.615(12)	1.614(15)	1.624(4)
<T2–O>		1.625(3)	1.613(10)	1.601(13)	1.597(13)	1.599(13)	1.599(14)	1.595(14)	1.594(14)	1.586(17)	1.630(4)
T3	O1	1.616(3)	1.597(11)	1.601(13)	1.602(14)	1.603(14)	1.606(15)	1.604(14)	1.602(15)	1.595(14)	1.626(4)
	O3	1.6071(17)	1.613(5)	1.589(9)	1.596(11)	1.590(10)	1.591(10)	1.571(10)	1.585(10)	1.608(9)	1.612(3)
	O6A	1.623(3)	1.621(8)	1.604(12)	1.615(12)	1.602(12)	1.599(13)	1.609(14)	1.611(12)	1.601(12)	1.623(5)
	O6B	1.602(4)	1.607(10)	1.606(12)	1.601(13)	1.607(12)	1.606(13)	1.602(14)	1.600(13)	1.590(13)	1.605(6)
<T3–O>		1.612(3)	1.610(9)	1.600(12)	1.604(13)	1.601(12)	1.601(13)	1.597(13)	1.600(13)	1.599(12)	1.617(5)

[a] With the crystal in the DAC without *P*-medium

[b] With the crystal in air after decompression

displacement parameters were refined by grouping all of the T-sites and all of the O-sites (Table 2). Refined atomic positions, displacement parameters and bond distances are reported in Tables 2 and 4. The structural refinement based on the data collected with the crystal in air after decompression showed that the *P*-induced structural evolution up to 8.45(5) GPa is completely reversible (Tables 1, 2, 3, 4); the refined Flack parameter was $x = 0.60(5)$.

Elastic behaviour

The evolution of the lattice parameters of $CsAlSi_5O_{12}$ with pressure is shown in Fig. 4. No phase transition has been observed within the pressure range investigated. In order to describe the elastic behaviour of this synthetic zeolite, the unit-cell volume data were fitted with a third-order Birch–Murnaghan equation-of-state (III-BM-EoS) (Birch 1947; Angel 2000) using the EOS-FIT5.2 program (Angel 2001). The BM-EoS parameters, refined using the data weighted by the uncertainties in P and V, are: $V_0 = 1{,}155(4)$ Å^3, $K_{T0} = 20(1)$ GPa and $K' = 6.5(7)$ (i.e. $K_{T0} = -V_0(\partial P/\partial V)_{P=0} = 1/\beta$, where β is the volume compressibility coefficient, and K' the pressure derivatives of the bulk modulus, $K' = \partial K_{T0}/\partial P$). "Axial moduli" were calculated with a third-order linearized BM-EoS (Angel 2000), substituting the cube of the individual lattice parameter (a^3, b^3, c^3) for the volume. The refined axial-EoS parameters are: $a_0 = 16.701(44)$ Å, $K_{T0a} = 14(2)$ GPa, $K'_a = 6.2(8)$ for the a-axis; $b_0 = 13.778(20)$ Å, $K_{T0b} = 21(3)$ GPa, $K'_b = 10(2)$ for the b-axis; $c_0 = 5.018(7)$ Å, $K_{T0c} = 33(3)$ GPa, $K'_c = 3.2(8)$ for the c-axis. The "linear-K_{T0j}", or "axial-K_{T0j}", is related to the linear-axial compressibility coefficient (β_j) by: $\beta_j = -1/(3K_{0j}) = (1/l_{0j})(\partial l_j/\partial P)$, where l_{0j} ($j = a, b, c$) is the length of the unit-cell axis under room conditions (i.e. $\beta_a = 0.024(3)$, $\beta_b = 0.015(2)$ and $\beta_c = 0.010(1)$ GPa^{-1}, with $\beta_a{:}\beta_b{:}\beta_c \approx 2.4{:}1.5{:}1$). The relationship between the linearised bulk moduli along the crystallographic axis ($K_{T0a}{:}K_{T0b}{:}K_{T0c} = 1{:}1.50{:}2.36$) shows an anisotropic elastic behaviour of this compound.

The diffraction data collected during decompression showed a complete reversibility of the elastic behaviour and the restoration of the lattice constants (Table 1).

Structural change with increasing pressure

For easy of understanding, the description of the process has been divided into two main stages (Fig. 3): from P_0 to P_1 (1.58(3) GPa) and from P_1 to P_7 (8.45(5) GPa). In both stages, tetrahedra behave as rigid units, as no significant changes in T–O distances occur (Table 4). T positions only show small shifts and so the structural change can be mainly assigned to adjustments of O atom positions (Table 2) due to rigid body rotations of tetrahedra. Within the investigated pressure range, the CAS framework structure (Baerlocher et al. 2001) is retained.

Structural changes up to 1.58(3) GPa

Major structural changes occur within the first compression stage (P_0 to P_1) at which certain $(Al,Si)O_4$ tetrahedra

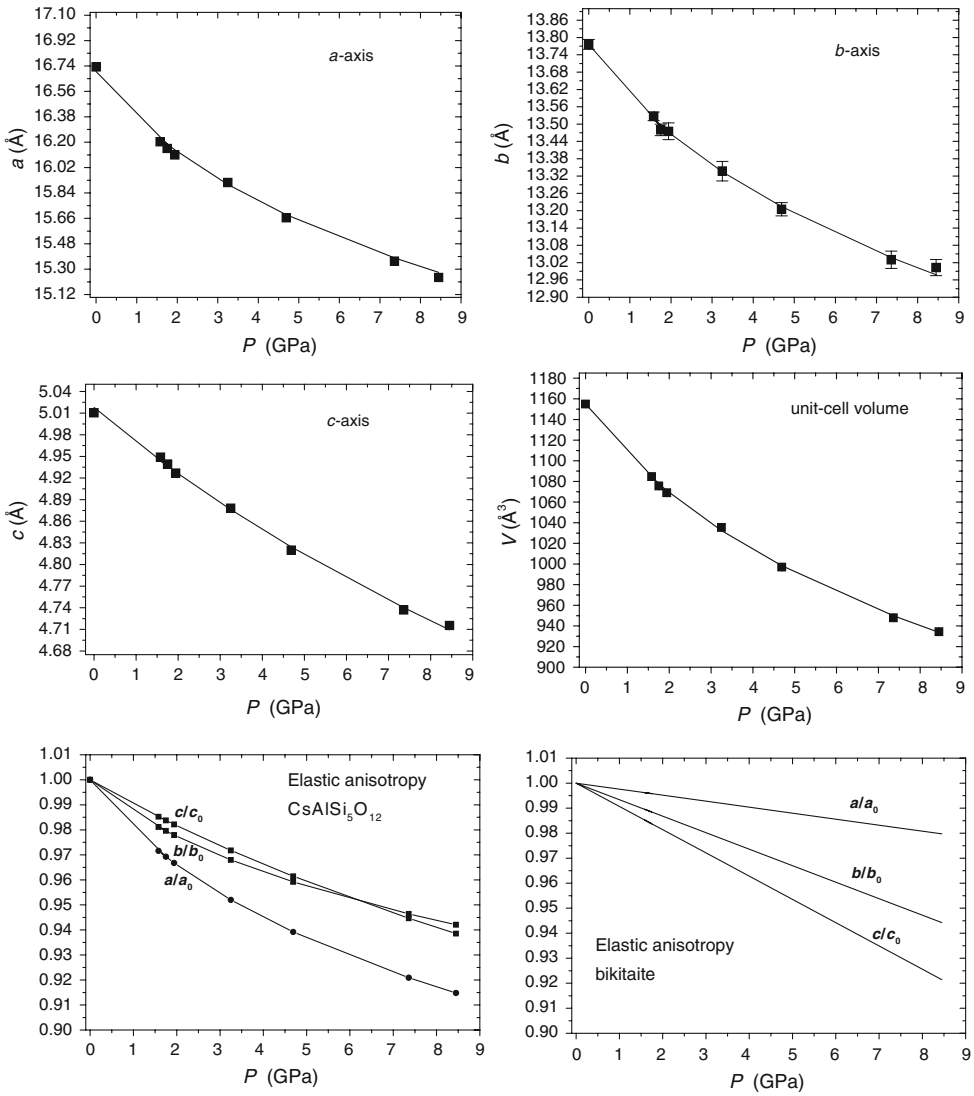

Fig. 4 Variation of the unit-cell parameters of $CsAlSi_5O_{12}$ as a function of pressure with axial and volume III-BM-EoS fit (*solid lines*) and elastic anisotropy in $CsAlSi_5O_{12}$ and bikitaite (Comodi et al. 2003; Gatta et al. 2003). For *a*, *c* and *V*, the *esd* values are smaller than the size of the *symbols*. Notice that in $CsAlSi_5O_{12}$ channels run parallel to the *c*-axis and in bikitatite parallel to the *b*-axis

undergo extensive rotation. For T1, the rotation axis is defined through the tetrahedron's center (T1) and the apex O2. For T2, the rotation axis bisects the O4–O4 and the O1–O2 edge, respectively. T3–O1 bond (Fig. 5) is the rotation axis of the T3 tetrahedron. Structural changes in this lower-pressure regime are dominated by rigid rotations of T1 and T3 tetrahedra, both rotating by about 30° around their respective axes. The rotation angle at different pressure has been estimated from tetrahedral projections parallel to the individual rotation axis. A relatively small rotation of the T2 tetrahedron (about 10°) results in a slight adjustment of O1 and O2 positions, and as a result, the rotation axes of T1 and T3 become slightly inclined. However, this effect is subordinate to the effects of the rotations of the T1 and T3 tetrahedra. As a consequence, a pronounced compression is observed for T1–O6B–T3 from 159(1)° to 135(1)° inducing a rapid flip of the T1–O5–T1-angle from 210(1)° (= 360° − 150°) to 140(2)°. This means that the obtuse and acute orientations of the T1–O5–T1 angle interchange. Coupled with the angle flip is a shift of O5 by almost 1 Å along the *c*-axis (Figs. 3, 5). In addition, counter clockwise rotation of adjacent T3 tetrahedra (linked by O3) leads to a flip of the orientation of the acute T3–O3–T3 angle (Fig. 3). Associated with these strong tetrahedral rotations at stage one, the CAS framework structure shows the steepest compressional gradient along all three axes within the examined pressure range. However, the compression is anisotropic and the *a*-axis shortens by ∼3.17%, the *b*-axis by ∼1.81% and the *c*-axis by ∼1.23% (Table 1).

Structural changes between 1.58(3) GPa and 8.45(5) GPa

In general, any structural change within this second compression stage is less pronounced than the atomic shifts imposed by increasing the pressure from ambient conditions to 1.58(3) GPa. In the second compression stage

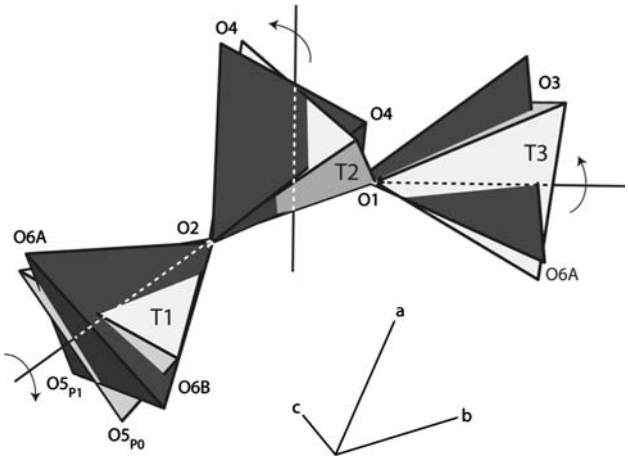

Fig. 5 Pressure induced structural deformation from P_0: 0.0001 GPa (*light grey*) to P_1: 1.58(3) GPa (*dark grey*). Rotation axes are drawn as black lines (*dotted inside tetrahedra*) with arrows indicating rotating direction. Rotations around axes are estimated as 30° for T1 and T3 and 10° for T2. Rotation of T1 and T3 are responsible for the significant shift of O5, mainly along the *c*-axis (from $O5_{P0}$ to $O5_{P1}$)

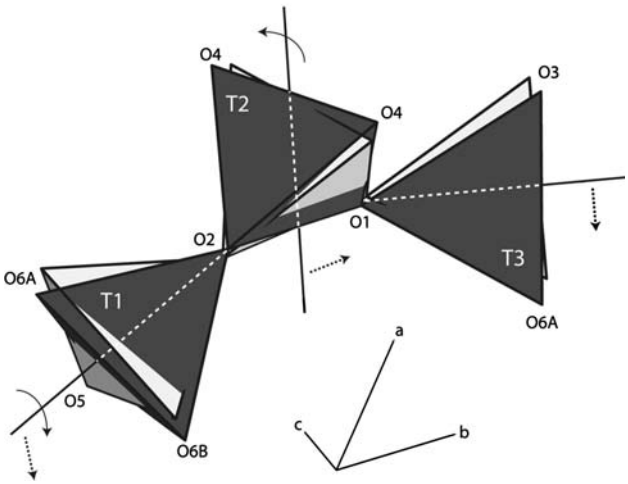

Fig. 6 Pressure induced structural deformation from P_1: 1.58(3) GPa (*light grey*) to P_7: 8.45(5) GPa (*dark grey*). Rotation axes are black lines (*dotted inside tetrahedra*) with arrows indicating rotating direction. Rotation of T1 and T2 around the axes are roughly 6°, T3 does not rotate. From P_1 to P_7, the rotation axes of all tetrahedra are also displaced (*along dotted arrows*). As a result, rigid-body tetrahedra perform movements comparable to a swinging bell

(from P_1 to P_7), rotations of T1 and T2 tetrahedra are very small (both approximately 6°) and T3 tetrahedron no longer rotates. In addition, all rotation axes (also the former rotation axis of T3) become further inclined (Fig. 6). This change in inclination is caused by a combination of T2 rotation, adjusting O1 and O2, and rotation of T1. Consequently, all tetrahedra perform slight movements comparable to the one of a swinging bell, which means that a rigid tetrahedron does not rotate about its center of gravity but it tilts around one tetrahedral apex. This mechanism compresses the T1–T2–T3-chain along the *b*-axis (Fig. 7). Bending of the T1–O2–T2-angle is still more pronounced than of T2–O1–T3 (Table 3; Fig. 8), leading to a kink of the T1–T2–T3 segment at O2, resulting in a more triangular cross-section of the Cs-occupied channel along [001] at higher pressure (Fig. 3). Only in this pressure range does the elliptical channel deform, with Cs–O distances decreasing (Fig. 9; Table 5).

The *a*-axis further compresses, but at a reduced rate compared with the initial deformation stage. This behaviour is consistent with only small changes of the T3–O3–T3- and T1–O5–T1- angle from P_1 to P_7 (Table 3). Along [001], the T2–T2–T2 chains respond to compression by bending at O4 due to continued rotation and the swinging-bell movement, but angular changes for T2-O4-T2 are small (Table 3; Fig. 7).

Structural evolution and anisotropy of compression

Continuous chains of… –T3–T1–T1–T3–T3–T1–T1–T3–… tetrahedra extend along [100] (Fig. 3). With the constraint of rigid body behaviour for tetrahedra, compression of the *a*-axis can only be due to tetrahedral rotations resulting in increased kinking of T–O–T-angles (Table 3; Fig. 8) and accompanying folding of the whole chain (Fig. 3).

If a chain of rigid tetrahedra is compressed in one direction, it must extend along another direction. Compression along the *b*-axis is compensated by shortening and bending the segment T1–T2–T3. It seems that rotation of T2 (Fig. 3, 5), with a rotation axis slightly inclined to the *a*-axis (passing through the tetrahedral edges O1–O2 and opposite O4–O4), is the main motor for compression parallel to [010]. This T2 rotation influences T1–O2–T2– and T2–O1–T3-angles (Fig. 8) and causes minor displacement of the T1 rotation axis influencing T1–O5–T1-, T3–O6A–T1- and T3–O6B–T1-angles (Fig. 8).

The lowest compression is measured along [001], the channel direction, where structure of $CsAlSi_5O_{12}$ contains two types of continuous chains of tetrahedra. One consists of… –T3–O6A–T1–O6B–T3–… and the other is a so-called pyroxene-type chain… –T2–O4–T2–O4–T2–… (Gottardi and Galli 1985). Compression of this chain along the *c*-axis (Fig. 7), expressed by bending the angle T2–O4–T2 (Table 3, Fig. 8), is low due to the limited T2-rotation. The contribution of the other chain… –T3–T1–T3–… to the stability of $CsAlSi_5O_{12}$ along [001] is likely to be much smaller than that of the pyroxene-type chains, as rotation axes of T1 and T3 are favourably aligned to accommodate pressure along [001] (Fig. 5), and this chain is already influenced by deformation of the *a* and *b* axes. T1 and T3 tetrahedra are corner-linked by oxygens O6A and O6B.

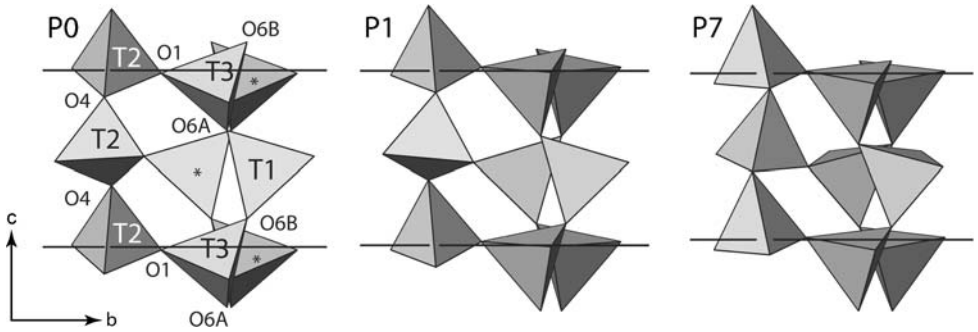

Fig. 7 T2-T2-T2-chains (pyroxene-type chains) and T3-T1-T3-chains projected along the *a*-axis at pressures P_0: 0.0001 GPa, P_1: 1.58(3) GPa and P_7: 8.45(5) GPa. The unlabeled chain marked with asterisks is symmetrically equivalent to T3-T1-T3, but on a lower level along [100]. With increasing pressure, these chains become more overlapped. *Horizontal black lines* represent unit-cell borders along [001]

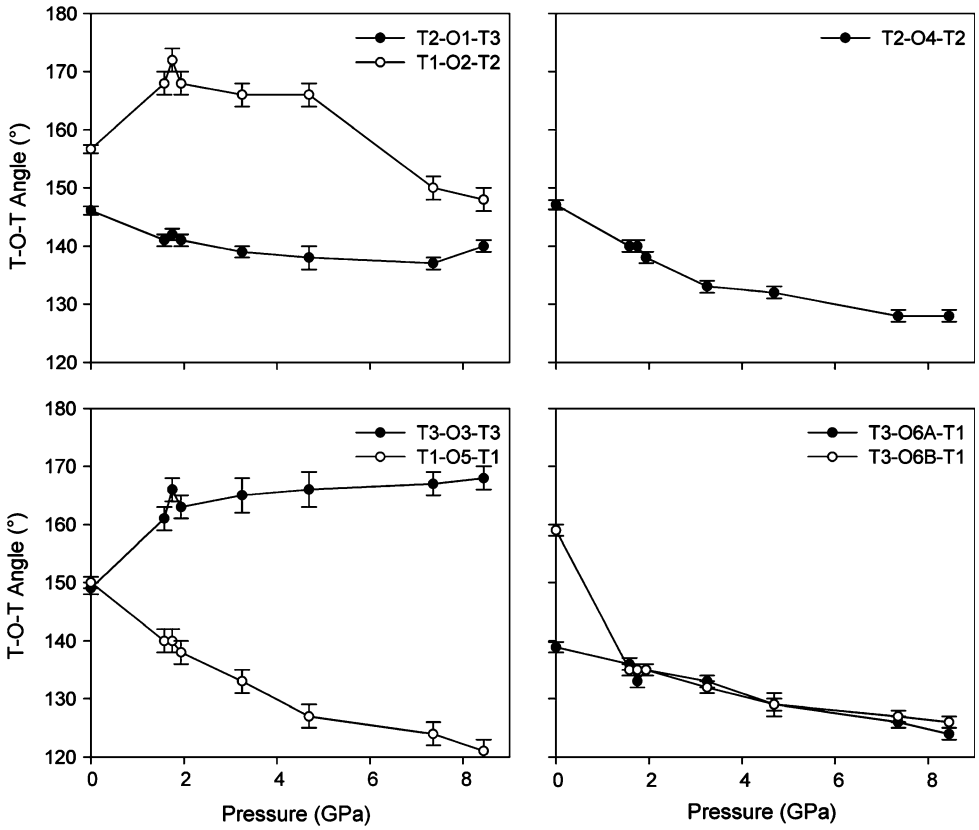

Fig. 8 T-O-T inter-tetrahedral bond angles at different pressure

At P_0, the T1–O6B–T3-angle is 159(1)° whereas the T1–O6A–T3-angle is 138.9(9)°. At P_1, both angles become similar (135(1)° and 136(1)°, respectively) (Fig. 8, Table 3). These changes mean that with increasing pressure, the fragment T3–O6B–T1 bends, and adopts a similar deformation as T3–O6A–T1 (Fig. 7). Figure 7 also demonstrates that due to the link T3–T1–T3, identical rotation directions of T3 tetrahedra (enclosing T1) around an axis nearly parallel to the *b*-axis are responsible for a counter-clockwise rotation of T1 around an axis of approximately corresponding orientation. When projected onto (100), equivalent T1–T3–T1-chains at different *x*-levels are now overlapped in a space-saving manner (Fig. 7).

Discussion and conclusions

$CsAlSi_5O_{12}$ remains crystalline at least up to 8.5 GPa and *P*-induced structural changes appear to be completely reversible (Tables 1, 2, 3, 4).

The analysis of the elastic behaviour described here shows that $CsAlSi_5O_{12}$ is considerably more compressible

Table 5 Mean Cs–O distances at various pressure (with $Cs–O_{max} \leq Cs–Si_{shortest}$)

P (GPa)	<Cs–O > (Å)
0.0001[a]	3.644
1.58(3)	3.656
1.75(4)	3.641
1.94(4)	3.605
3.25(4)	3.529
4.69(5)	3.461
7.36(6)	3.327
8.45(5)	3.297

[a] With the crystal in the DAC without *P*-medium

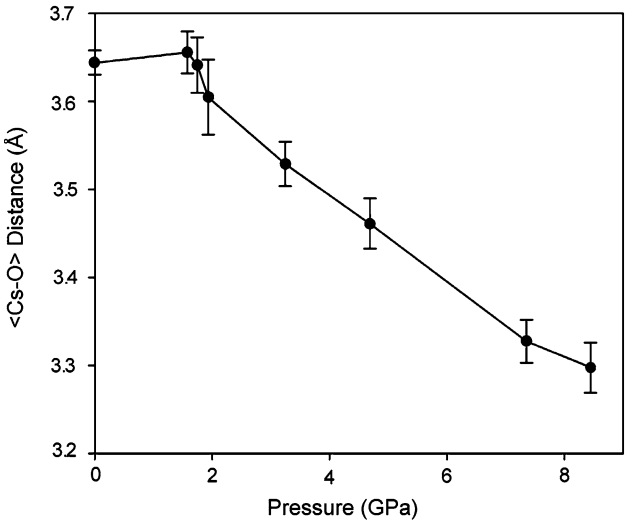

Fig. 9 Average Cs–O bond lengths at different pressure

than natural bikitaite (K_{T0}(bikitaite) = 44.2(4), K_{T0}($CsAlSi_5O_{12}$) = 20(1) GPa). These two open-framework silicates show strong structural homologies since their tetrahedral frameworks are made up of the same building blocks (Fig. 1). The general configuration of the channels is similar: 8mR-channels//[010] in bikitaite (Comodi et al. 2003, Gatta et al. 2003, Fig. 2) and // [001] in $CsAlSi_5O_{12}$ (Fig. 3) and the "framework density" (FD, Baerlocher et al. 2001) is FD = 20.3 tetrahedra/1,000 Å in bikitaite and FD = 20.6 tetrahedra/1000 $Å^3$ in $CsAlSi_5O_{12}$. The different elastic anisotropy and volume compressibility of bikitaite and $CsAlSi_5O_{12}$ (Fig. 4) might be due to the different configuration of the tetrahedral framework or, more likely, to the different content of their channels. In bikitaite, the extra-framework content is represented by $2Li + 2H_2O$ molecules (Fig. 2); in $CsAlSi_5O_{12}$ by only one Cs-site (Fig. 3). In other words, the channels in bikitaite are more stuffed than in $CsAlSi_5O_{12}$, resulting in a lower compressibility of the channels and, as a consequence, of the entire structure of the former.

The main structural changes in $CsAlSi_5O_{12}$ occur at $P < 2$ GPa and involve major rigid rotations of tetrahedra. At $P > 2$ GPa, some contributions to the compressional mechanisms acting at low-*P* appear to reach a limit, as shown by the behaviour of T2–O1–T3 and T3–O3–T3 angles with *P* (Fig. 8; Table 3). However, the structural rearrangements within the entire *P*-range investigated appear to be driven by continuous mechanisms, with no transitional behaviour, as confirmed by the continuous and monotonic evolution of the lattice parameters with *P* and conservation of *Ama*2 symmetry. Changes in compressional mechanisms in absence of phase-transitions have been reported for several open-framework silicates (Allan and Angel 1997; Tribaudino et al. 1999; Benusa et al. 2005; Gatta et al. 2005, 2006; Gatta and Wells 2006; Gatta and Angel 2007).

The origins of the elastic anisotropy in $CsAlSi_5O_{12}$ have been described in the previous section in detail: the two independent chains running along [001] (i.e.… –T3–O6A–T1–O6B–T3–…and… –T2–O4–T2–O4–T2–…) and their limited ability to contract by kinking make the structure less compressible along the *c*-axis than along the *a*- and *b*-axes. Viewing the structure of $CsAlSi_5O_{12}$ down [001] and [010] (Fig. 3) it is apparent that the compressibility along the *c*-axis is hindered by the framework configuration, whereas along the *a*- and *b*-axis the presence of potentially compressible channels allow a higher compressibility.

The slightly higher compressibility of the structure along the *a*-axis than along the *b*-axis might be due to the bonding environment of the extra-framework cation and to the compression of the 8mR-channel, which is governed by the inter-tetrahedral T1–O5–T1 angle. At room conditions, the Cs-site lies off-center in the 8mR-channel with a coordination number CN = 13, $Cs–O_{max} \sim 3.609$ and $Cs–O_{min} \sim 3.940$ Å (with $Cs–Si_{min} \sim 4.02$ Å) (Fig. 3). The oxygens belonging to the opposite part of the channel wall with respect to the Cs atom are not bonded to it. Compression of the tetrahedral framework leads to a continuous change in the bonding environment. At 1.58 GPa, the CN = 15 ($Cs–O_{max} \sim 3.860$ and $Cs–O_{min} \sim 3.426$ Å, with $Cs–Si_{min} \sim 3.86$ Å), at 4.69 GPa it decreases to CN = 14 ($Cs–O_{max} \sim 3.689$ and $Cs–O_{min} \sim 3.186$ Å, with $Cs–Si_{min} \sim 3.71$ Å) and at 8.45 GPa the CN = 12 ($Cs–O_{max} \sim 3.426$ and $Cs–O_{min} \sim 3.061$ Å, with $Cs–Si_{min} \sim 3.59$ Å) (Fig. 9). In other words, there is an increase of Cs–O bond strengths with *P* to oxygens lying on the same side as Cs in the 8mR-channel, whereas there is a loss of bonding to the oxygens lying on the opposite side. Hence, there are two counterbalanced effects in response to the pressure: (1) along [100] the channel tends to be compressed symmetrically (because of symmetry), with a shortening of the Cs-O bond lengths and a strong T1–O5–T1 inter-tetrahedral tilting (Table 3), and (2) along [010] the channel is compressed asymmetrically, because of the off-center location and the bonding environment of

the Cs-site. As a consequence, the channel changes its shape toward a triangular cross-section (Fig. 3), with the most acute internal angle corresponding to the channel side with no Cs-O interactions, and the compressibility along [100] is slightly higher than along [010].

At high-temperature, the structure of $CsAlSi_5O_{12}$ behaves anisotropically, with $\alpha(c) \gg \alpha(a) > \alpha(b)$ between 25 and 180°C, whereas $\alpha(c) \gg \alpha(b) > \alpha(a)$ between 180 and 500°C. This confirms that along [001] the structure tends to expand more than along [010] and [100]. In other words, the H*P*/H*T*-mechanisms based on tetrahedral tilting with effects along [001] lead to a structural configuration energetically more stable only upon heating, with an increase of the T–O–T angles and a consequent expansion of the *c*-axis. Under hydrostatic compression, the structure reacts with a lower compressibility along [001] than on (001), because the axial compression along [001] *via* tetrahedral tilting is energetically more costly.

The high thermo-elastic stability of $CsAlSi_5O_{12}$, the immobility of Cs at H*T*/H*P*-conditions (Fisch et al. 2008 and this study), the preservation of crystallinity at least up to 8.5 GPa and 1000°C in elastic regime and the extremely low leaching rate of Cs from $CsAlSi_5O_{12}$ (which is three orders of magnitude lower than the leaching rate of Cs from boro-silicate glass, Bubnova et al. 2007) make this open-framework silicate a possible candidate for use in the immobilization of radioactive isotopes of Cs.

Acknowledgments This work was funded by the Italian Ministry of University and Research, MIUR-Project: 2006040119_004 (grant to Alessandro Pavese). T.A. acknowledges support by the Swiss National Science Foundation, grant 200020-112198 "Crystal Chemistry of Minerals". The authors thank Mr Bruno Pafundi for helping in the set-up of the high-pressure laboratory of crystallography at the Dipartimento di Scienze della Terra, Università degli Studi di Milano-Italy. The Editor Milan Rieder, Mark Welch and an anonymous reviewer are thanked.

References

Adl T, Vance ER (1982) $CsAlSi_5O_{12}$: a possible host for ^{137}Cs immobilization. J Mater Sci 17:849–855

Allan DR, Angel RJ (1997) A high-pressure structural study of microcline ($KAlSi_3O_8$) to 7 GPa. Eur J Mineral 9:263–275

Angel RJ (2000) Equation of state. In: Hazen RM, Downs RT (eds) High-temperature and high-pressure crystal chemistry, vol 41, pp 35–59. Reviews in Mineralogy and Geochemistry, Mineralogical Society of America and Geochemical Society, Washington, USA

Angel RJ (2001) EoSFit v6.0. Computer program. Crystallography Laboratory, Dept. Geological Sciences, Virginia Tech, Blacksburg, USA. http://www.crystal.vt.edu

Angel RJ (2002) Absorb v5.2. Computer program. Crystallography Laboratory, Dept. Geological Sciences, Virginia Tech, Blacksburg, USA, http://www.crystal.vt.edu

Angel RJ, Allan DR, Miletich R, Finger LW (1997) The use of quartz as an internal pressure standard in high-pressure crystallography. J Appl Crystallogr 30:461–466

Angel RJ, Bujak M, Zhao J, Gatta GD, Jacobsen SD (2007) Effective hydrostatic limits of pressure media for high-pressure crystallographic studies. J Appl Crystallogr 40:26–32

Annehed H, Fälth L (1984) The crystal structure of $Cs_{0.35}Al_{0.35}Si_{2.65}O_6$, a cesium-aluminosilicate with the bikitaite framework. Z Kristallogr 166:301–306

Araki T (1980) Crystal structure of a cesium aluminosilicate, $Cs[AlSi_5O_{12}]$. Z Kristallogr 152:207–213

Baerlocher Ch, Meier WM, Olson DH (2001) Atlas of zeolite framework types, Fifth Revised Version. Elsevier, Amsterdam

Beger RM (1969) Crystal structure and composition of pollucite. Z Kristallogr 129:280–302

Benusa MT, Angel RJ, Ross NL (2005) Compression of albite, $NaAlSi_3O_8$. Am Mineral 90:1115–1120

Birch F (1947) Finite elastic strain of cubic crystal. Phys Rev 71:809–824

Bissert G, Liebau FN (1986) The crystal structure of a triclinic bikitaite, $LiAlSi_2O_6{\cdot}H_2O$. N Jb Miner Mh 6:241–252

Bubnova RS, Krzhizhanovskaya MG, Filatov SK, Ugolkov VL, Paufler P (2007) XRD and DSC study of the formation and the melting of a new zeolite-like borosilicate CsBSi5O12 and (Cs, Rb) BSi5O12 solid solutions. Z Kristallogr 222:83–88

Burnham CW (1966) Computation of absorption corrections and the significance of end effects. Am Mineral 51:159–167

Comodi P, Zanazzi PF, Weiss Z, Rieder M, Drábek M (1999) Cs-tetra-ferri-annite: high-pressure and high-temperature behaviour of a potential nuclear waste disposal phase. Am Mineral 84:325–332

Comodi P, Gatta GD, Zanazzi PF (2003) Effects of pressure on the structure of bikitaite. Eur J Mineral 15:247–255

Drábek M, Rieder M, Viti C, Weiss Z, Frýda J (1998) Hydrothermal synthesis of a Cs ferruginous trioctahedral mica. Can Mineral 36:755–761

Ferro O, Quartieri S, Vezzalini G, Fois E, Gamba A, Tabacchi G (2002) High-pressure behaviour of bikitaite: an integrated theoretical and experimental approach. Am Mineral 87:1415–1425

Firor RL, Seff K (1977) Zero-coordinate K^+. Crystal structure of dehydrated cesium and potassium exchanged zeolite A, Cs_7K_5-A. J Am Chem Soc 99:6249–6253

Fisch M, Armbruster Th, Kolesov B (2008) Temperature-dependent structural study of microporous $CsAlSi_5O_{12}$. J Solid State Chem 181:423–431

Fois E, Tabacchi G, Quartieri S, Vezzalini G (1999) Dipolar host/guest interactions and geometrical confinement at the basis of the stability of one-dimensional ice in zeolite bikitaite. J Chem Phys 111:355–359

Gallagher SA, McCarthy GJ, Smith DK (1977) Preparation and X-ray characterization of $CsAlSiO_4$. Mater Res Bull 12:1183–1190

Gatta GD, Comodi P, Zanazzi PF (2003) New insights on high-pressure behaviour of microporous materials from X-ray single crystal data. Micropor Mesopor Mater 61:105–111

Gatta GD, Comodi P, Zanazzi PF, Boffa Ballaran T (2005) Anomalous elastic behavior and high-pressure structural evolution of zeolite levyne. Am Mineral 90:645–652

Gatta GD, Nestola F, Boffa Ballaran T (2006) Elastic behavior, phase transition and pressure induced structural evolution of analcime. Am Mineral 91:568–578

Gatta GD, Wells SA (2006) Structural evolution of zeolite levyne under hydrostatic and non-hydrostatic pressure: geometric modelling. Phys Chem Minerals 33:243–255

Gatta GD, Angel RJ (2007) Elastic behavior and pressure-induced structural evolution of nepheline: implications for the nature of the modulated superstructure. Am Mineral 92:1446–1455

Gottardi G, Galli E (1985) Natural zeolites. Springer, Berlin

Hawthorne FC, Cooper MA, Simmons WB, Falster AU, Laurs BM, Armbruster T, Rossman GR, Peretti A, Günter D, Grobéty B

(2004) Pezzottaite Cs(Be2Li) Al2Si6O18. A spectacular new beryl-group mineral from the Sakavalana pegmatite, Fianarantsoa province, Madagascar. Min Rec 35:369–378

Hess FL, Fahey JJ (1932) Cesium biotite from Custer County, South Dakota. Am Mineral 17:173–176

Hughes RW, Weller MT (2002) The structure of the CAS type zeolite, $Cs_4[Al_4Si_{20}O_{48}]$ by high-resolution powder neutron diffraction and ^{29}Si MAS NMR. Micropor Mesopor Mater 51:189–196

Ito J (1976) Crystal synthesis of a new cesium alumosilicate, $CsAlSi_5O_{12}$. Am Mineral 61:170–171

Klaska R (1977) Hydrothermalsynthesen und Strukturuntersuchungen zu kationenabhängigen Veränderungen von aufgefüllten Tetraedergerüsten aus dem Bereich der Feldspäte und seiner Vertreter. PhD Dissertation, Universität Hamburg, Germany

Klika Z, Weiss Z, Mellini M, Drábek M (2006) Water leaching of cesium from selected cesium mineral analogues. Appl Geochem 21:405–418

Komarneni S, Roy R (1983) Hydrothermal reaction and dissolution Studies of $CsAlSi_5O_{12}$ in water and brines. J Am Ceramic Soc 66:471–474

Kocman V, Gait RI, Rucklidge J (1974) The crystal structure of bikitaite. Am Mineral 59:71–78

Mellini M, Weiss Z, Rieder M, Drábek M (1996) Cs-ferriannite as a possible host for waste cesium: crystal structure and synthesis. Eur J Mineral 8:1265–1271

Miletich R, Allan DR, Kuhs WF (2000) High-pressure single-crystal techniques. In: Hazen Rm, Downs RT (eds) High-temperature and high-pressure crystal chemistry, vol 41, pp 445–519. Reviews in Mineralogy and Geochemistry, Mineralogical Society of America and Geochemical Society, Washington, USA

Newnham RE (1967) Crystal structure and optical properties of pollucite. Am Mineral 52:1515–1518

Ni YX, Hughes JM (1996) The crystal structure of nanpingite—$2M_2$, the Cs end member of muscovite. Am Mineral 81:105–110

Oxford Diffraction (2005) Oxford diffraction Ltd., Xcalibur CCD system, CrysAlis Software system

Sheldrick GM (1997) SHELX-97. Programs for crystal structure determination and refinement. University of Göttingen, Germany

Taylor P, DeVaal S.D., Derrek G (1989) Owen Stability relationships between solid cesium aluminosilicates in aqueous solutions at 200°C. Can J Chem 67:76–81

Tribaudino M, Benna P, Bruno E, Hanfland M (1999) High pressure behavior of lead feldspar ($PbAl_2Si_2O_8$). Phys Chem Minerals 26:367–374

Vance TB, Seff K (1975) Hydrated and dehydrated crystal structure of seven-twelfths cesium exchanged zeolites A. J Phys Chem 79:2163–2166

Vance ER, Cartz L, Karioris FG (1984) X-ray diffraction and leaching of $CsAlSi_5O_{12}$ and $CsZr_2(PO_4)_3$ irradiated by argon (3 MeV) ions. J Mater Sci 19:2943–2947

Wilson AJC, Prince E (eds) (1999) International tables for X-ray Crystallography, volume C: Mathematical, physical and chemical tables, 2nd edn. Kluwer, Dordrecht

Zanardi S, Alberti A, Cruciani G, Corma A, Fornés V, Brunelli M (2004) Crystal structure determination of zeolite Nu-6(2) and its layered precursor Nu-6(1). Angew Chemie (Int Ed) 43:4933–4937